

The Tensor Pomeron and Low- x Deeply Virtual Compton Scattering *

PIOTR LEBIEDOWICZ, ANTONI SZCZUREK

Institute of Nuclear Physics Polish Academy of Sciences, Radzikowskiego 152,
PL-31342 Kraków, Poland

OTTO NACHTMANN

Institut für Theoretische Physik, Universität Heidelberg, Philosophenweg 16,
D-69120 Heidelberg, Germany

The two-tensor-pomeron model is applied to deeply virtual Compton scattering (DVCS) on a proton. A good description of the DVCS HERA data at small Bjorken- x is achieved due to a sizeable interference of soft and hard pomeron contributions. We present two fits which differ somewhat in the strength of the hard pomeron contribution. We describe, in the same framework, both the low Q^2 and high Q^2 regimes and the transition between them. We find that the soft-pomeron contribution is considerable up to $Q^2 \sim 20 \text{ GeV}^2$. The reggeon exchange term is particularly relevant for describing the scattering of a real photon on a proton measured at lower γp energies at FNAL. We find that the ratio of $\gamma^* p \rightarrow \gamma p$ cross-sections for longitudinally and transversely polarized virtual photons strongly increases with t . Our findings may be checked in future lepton-nucleon scattering experiments in the low- x regime, for instance, at a future Electron-Ion Collider (EIC) at the BNL and LHeC at the LHC.

1. Introduction

This presentation summarizes some of the key results of [1] to which we refer the reader for further details. We apply the two-tensor-pomeron model [2] to deeply virtual Compton scattering (DVCS) on the proton, $\gamma^* p \rightarrow \gamma p$. Our model can be used for large $\gamma^* p$ c.m. energy $W \gg m_p$, $\sqrt{|t|}$, $|t| \lesssim 1 \text{ GeV}^2$, and small Bjorken- x , say $x = Q^2/(W^2 + Q^2 - m_p^2) < 0.02$.

* Presented by P. Lebedowicz at XXIX Cracow Epiphany Conference on Physics at the Electron-Ion Collider and Future Facilities, Kraków, Poland, January 16-19, 2023.

Here m_p is the proton mass, Q^2 is the photon virtuality, and t is the squared momentum transfer at the proton vertex.

The DVCS has been a subject of extensive experimental and theoretical research; see Sec. 1 in [1]. Experimental program at the Electron-Ion Collider (EIC) [4], and, if realized, at the Large Hadron Electron Collider (LHeC) at the LHC [5], are expected to improve our knowledge of DVCS in a wide kinematic range.

DVCS is a prime playground for the application of the generalized parton-distribution (GPD) concept based on perturbative QCD (pQCD), cf. [3] for a review. Here we discuss DVCS in the Regge approach where the scattering is described using exchange objects. In the tensor-pomeron model, introduced for soft high-energy reactions in [6] and extended to hard reactions in [2], the charge-conjugation $C = +1$ soft (\mathbb{P}_1) and hard (\mathbb{P}_0) pomeron and the reggeons ($\mathbb{R}_+ = f_{2\mathbb{R}}, a_{2\mathbb{R}}$) are described as effective rank-2 symmetric tensor exchanges.

A two-pomeron description of low- x DIS was first proposed in [8]. However, there a vector nature of the pomerons was considered. It was shown in [2] that considering these two pomerons as vector objects leads to the conclusion that they decouple in the total photoabsorption cross-section on the proton and in the structure functions of low- x DIS. But experiment clearly shows pomeron-exchange behaviour for these quantities at large W ; see Fig. 5 of [2].

Applications of the tensor-pomeron approach were given for a number of exclusive central-production reactions, see e.g. [9–15], and for soft-photon radiation [16–18] in hadron-hadron collisions. For some remarks on the history of tensor-pomeron concepts and corresponding references see [7]. It is worth mentioning that the tensor-pomeron current (Eq. (2.3) of [7]) cannot be universally proportional to the energy-momentum tensor.

2. Formalism

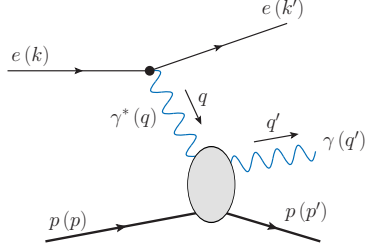
We investigate the real and deeply virtual Compton scattering on a proton

$$\gamma^{(*)}(q, \epsilon) + p(p, \lambda) \rightarrow \gamma(q', \epsilon') + p(p', \lambda'). \quad (1)$$

The momenta are indicated in brackets, $\lambda, \lambda' \in \{1/2, -1/2\}$ are the proton helicities, and ϵ, ϵ' are the photon polarization vectors. For an initial virtual photon γ^* the reaction (1) is extracted from $ep \rightarrow ep\gamma$ scattering (see Fig. 1)

$$e(k) + p(p, \lambda) \rightarrow e(k') + \gamma(q', \epsilon') + p(p', \lambda'). \quad (2)$$

Here the Bethe-Heitler process and DVCS contribute with the latter corresponding to electroproduction of the γp state. We assume for (2) unpo-


 Fig. 1. DVCS contribution to $ep \rightarrow ep\gamma$ (2).

larized initial particles and no observation of the polarization of final state particles. The standard kinematic variables are (see Table 1 of [19])

$$q = k - k', \quad q^2 = -Q^2, \quad s = (p + k)^2, \quad t = (p - p')^2, \quad W^2 = (p + q)^2, \\ x = \frac{Q^2}{2p \cdot q} = \frac{Q^2}{W^2 + Q^2 - m_p^2}, \quad y = \frac{p \cdot q}{p \cdot k} = \frac{W^2 + Q^2 - m_p^2}{s - m_p^2}. \quad (3)$$

Adapting (3.20) and (3.21) of [19] to the reaction (2) and integrating over the azimuthal angle φ defined in (2.1) of [19] we get for the DVCS part:

$$\frac{d\sigma(ep \rightarrow ep\gamma)}{dydQ^2dt} = \Gamma_{ep\gamma} \left(\frac{d\sigma_T}{dt}(Q^2, W^2, t) + \varepsilon \frac{d\sigma_L}{dt}(Q^2, W^2, t) \right) \quad (4)$$

with $\Gamma_{ep\gamma}$ the γ^* flux factor [1]. The differential cross-sections for $\gamma^*p \rightarrow \gamma p$ for transverse and longitudinal polarization of the γ^* are

$$\frac{d\sigma_T}{dt}(Q^2, W^2, t) = \frac{1}{2} \left(\frac{d\sigma_{++}}{dt}(Q^2, W^2, t) + \frac{d\sigma_{--}}{dt}(Q^2, W^2, t) \right), \\ \frac{d\sigma_L}{dt}(Q^2, W^2, t) = \frac{d\sigma_{00}}{dt}(Q^2, W^2, t), \quad (5)$$

where

$$\frac{d\sigma_{mm}}{dt}(Q^2, W^2, t) = \frac{1}{16\pi(W^2 - m_p^2)\sqrt{(W^2 - m_p^2 + Q^2)^2 + 4m_p^2Q^2}} \\ \times \frac{1}{2} \sum_{\lambda, \lambda', a} \left| \langle \gamma(q', \epsilon'_a), p(p', \lambda'), \text{out} | eJ_\mu(0)\epsilon_m^\mu | p(p, \lambda) \rangle \right|^2. \quad (6)$$

Here eJ_μ is the electromagnetic current, $\epsilon_m(m = \pm, 0)$ are the standard γ^* polarization vectors for right and left circular and longitudinal polarization (see (3.11)–(3.14) of [19]) and $\epsilon'_a(a = 1, 2)$ are the polarization vectors of the real photon in the final state.

We describe the amplitude for (1) in terms of the $C = +1$ exchanges of soft (\mathbb{P}_1) and hard (\mathbb{P}_0) pomeron and the reggeons $f_{2\mathbb{R}}$ and $a_{2\mathbb{R}}$. We get

$$\begin{aligned} & \langle \gamma(q', \epsilon'), p(p', \lambda'), \text{out} | eJ_\nu(0)\epsilon^\nu | p(p, \lambda) \rangle \equiv (\epsilon'^\mu)^* \mathcal{M}_{\mu\nu, \lambda'\lambda} \epsilon^\nu \\ & = -(\epsilon'^\mu)^* \sum_{j=0,1} \Gamma_{\mu\nu\kappa\rho}^{(\mathbb{P}_j\gamma^*\gamma^*)}(q', q) \epsilon^\nu \Delta^{(\mathbb{P}_j)\kappa\rho, \alpha\beta}(W^2, t) \bar{u}_{\lambda'}(p') \Gamma_{\alpha\beta}^{(\mathbb{P}_j pp)}(p', p) u_\lambda(p) \\ & \quad + (\mathbb{P}_j \rightarrow f_{2\mathbb{R}}, a_{2\mathbb{R}}). \end{aligned} \quad (7)$$

Here $\Delta^{(\mathbb{P}_j)}$, $\Gamma^{(\mathbb{P}_j pp)}$, and $\Gamma_{\mu\nu\kappa\rho}^{(\mathbb{P}_j\gamma^*\gamma^*)}(q', q)$ denote the effective propagator, the proton vertex function, and the $\mathbb{P}_j\gamma^*\gamma^*$ ($j = 0, 1$) vertex, respectively, for the tensor pomerons \mathbb{P}_j . The *Ansätze* for the $f_{2\mathbb{R}}$ and $a_{2\mathbb{R}}$ reggeons ($j = 2$) are analogous. The properties of $\mathbb{P}_0, \mathbb{P}_1, f_{2\mathbb{R}}$, and $a_{2\mathbb{R}}$, and their couplings to protons and photons will be taken as in [2]. We get

$$\begin{aligned} \mathcal{M}_{\mu\nu, \lambda'\lambda} = & -i \sum_{j=0,1,2} \frac{3\beta_{jpp}}{2W^2} (-iW^2\alpha'_j)^{\alpha_j(t)-1} F_1^{(j)}(t) \bar{u}_{\lambda'}(p') \gamma^\kappa (p' + p)^\rho u_\lambda(p) \\ & \times \left[2a_{j\gamma^*\gamma^*}(q^2, 0, t) \Gamma_{\mu\nu\kappa\rho}^{(0)}(q', -q) - b_{j\gamma^*\gamma^*}(q^2, 0, t) \Gamma_{\mu\nu\kappa\rho}^{(2)}(q', -q) \right]. \end{aligned} \quad (8)$$

For the coupling constants β_{jpp} of the pomerons ($j = 0, 1$) and reegion ($j = 2$) to protons we take $\beta_{0pp} = \beta_{1pp} = 1.87 \text{ GeV}^{-1}$, $\beta_{2pp} = 3.68 \text{ GeV}^{-1}$. The pomeron and reggeon trajectory functions are assumed to be of linear form

$$\alpha_j(t) = \alpha_j(0) + \alpha'_j t, \quad \alpha_j(0) = 1 + \epsilon_j, \quad (j = 0, 1, 2). \quad (9)$$

The slope parameters α'_j are taken as the default values from [2]: $\alpha'_1 = \alpha'_0 = 0.25 \text{ GeV}^{-2}$, $\alpha'_2 = 0.9 \text{ GeV}^{-2}$. The intercept parameters of the trajectories (9) were determined from detailed comparison of the model with the DIS HERA data and photoproduction data in [2]:

$$\text{soft pomeron } \mathbb{P}_1 : \quad \epsilon_1 = 0.0935^{+76}_{-64}, \quad (10)$$

$$\text{hard pomeron } \mathbb{P}_0 : \quad \epsilon_0 = 0.3008^{+73}_{-84}, \quad (11)$$

$$\text{reggeon } \mathbb{R}_+ : \quad \alpha_2(0) = 0.485^{+88}_{-90}. \quad (12)$$

The coupling functions $a_{j\gamma^*\gamma^*}$ and $b_{j\gamma^*\gamma^*}$ in (8) are (see (2.21)–(2.23) of [1])

$$\begin{aligned} a_{j\gamma^*\gamma^*}(q^2, 0, t) &= e^2 \hat{a}_j(Q^2) F^{(j)}(t), \quad j = 0, 1, 2, \\ b_{2\gamma^*\gamma^*}(q^2, 0, t) &= e^2 \hat{b}_2(Q^2) F^{(2)}(t). \end{aligned} \quad (13)$$

Here, $\hat{a}_j(Q^2)$ and $\hat{b}_j(Q^2)$ were determined in [2] from the global fit to HERA inclusive DIS data for $Q^2 < 50 \text{ GeV}^2$ and $x < 0.01$ and the ($Q^2 = 0$) photoproduction data. All coupling functions \hat{a}_j and \hat{b}_j are plotted in Fig. 2 of [1].

For small Q^2 , the soft pomeron function $b_{1\gamma^*\gamma^*}$ gives a larger contribution to the cross-section than the corresponding hard one $b_{0\gamma^*\gamma^*}$. In the large Q^2 region the reverse is found. In Sec. 3, we shall show two alternative fits for $b_{1\gamma^*\gamma^*}$ and $b_{0\gamma^*\gamma^*}$ obtained from a comparison to HERA DVCS data.

We use the combined form-factor functions for a given j ($j = 0, 1, 2$)

$$F_{\text{eff}}^{(j)}(t) = F^{(j)}(t) \times F_1^{(j)}(t) = \exp(-b_j|t|/2), \quad (14)$$

assuming the same t dependence for both a and b coupling functions. We take $b_1 = b_2 = 5.0 \text{ GeV}^{-2}$ and $b_0 = 1.0 \text{ GeV}^{-2}$ from [1].

3. Results

We shall restrict our discussion to experimental results that satisfy the conditions $x \approx Q^2/W^2 < 0.02$ and $|t| \lesssim 1 \text{ GeV}^2$ where our model should be reliable.

In Fig. 2 we compare the tensor-pomeron model results, FIT 1 (left panel) and FIT 2 (right panel), to the FNAL data [20] on real-photon-proton scattering ($\gamma p \rightarrow \gamma p$), and to HERA data [21–24] on DVCS ($\gamma^*(Q^2)p \rightarrow \gamma p$) for different averaged W and Q^2 . The complete cross-section is a coherent sum of soft and hard components in the amplitude. For real Compton scattering ($Q^2 = 0$) the cross-section is dominated by soft-pomeron exchange with an additional contribution from reggeon exchange at lower energies. The hard-pomeron contribution is negligibly small there. The dominant contribution comes from the b -type coupling functions $b_{j\gamma^*\gamma^*}$ ($j = 0, 1$). Their size differs in the two fits. We see from the bottom panels of Fig. 2 that for higher Q^2 the soft component slowly decreases relative to the hard one. A significant constructive interference effect between the soft and hard components is clearly visible. Here and in the following, the interference term is calculated as the difference of coherent and incoherent cross-sections of the \mathbb{P}_1 , \mathbb{P}_0 , and \mathbb{R} contributions. The Fits 1 and 2 hardly differ for the W region where there are data. But for higher W values FIT 2, where the contribution from the hard pomeron is enhanced, gives a steeper rise of the cross-section with W and especially so for larger Q^2 . For FIT 1, we see that the soft pomeron survives to relatively large Q^2 and at $Q^2 \simeq 50 \text{ GeV}^2$ the interference term plays an important role in the description of the data.

In Fig. 3 we show the differential cross-sections $d\sigma/dt$ for different $\langle W \rangle$ and $\langle Q^2 \rangle$. We use

$$\frac{d\sigma}{dt} = \frac{d\sigma_{\text{T}}}{dt} + \varepsilon \frac{d\sigma_{\text{L}}}{dt} \quad (15)$$

with $\varepsilon = 1$ ($\varepsilon \approx 1$ for the HERA kinematic region). In the top panels of Fig. 3 the upper line corresponds to $W = 12.7 \text{ GeV}$ and $Q^2 = 0$ and

should be compared to the averaged FNAL data (top data points) for the $\gamma p \rightarrow \gamma p$ reaction [20]. In this kinematic range, for $Q^2 = 0$ and at intermediate W , the reggeon plus soft- \mathbb{P} contributions dominate and the hard- \mathbb{P} exchange gives a negligible contribution. As expected, there is a significant interference between the reggeon and soft-pomeron components. The slope parameters b_2 and b_1 in (14) are adjusted to the FNAL $d\sigma/dt$ data on the real-photon-proton scattering. At higher W and Q^2 measured at HERA the hard pomeron plays an increasingly important role. The slope parameter b_0 for the hard-pomeron exchange is adjusted to the DVCS HERA data. As we noted above, $d\sigma(\gamma^* p \rightarrow \gamma p)/dt$ is the sum of two contributions $d\sigma_T/dt$ and $d\sigma_L/dt$ with the latter term becoming very small for $|t| \rightarrow 0$. This is understandable since for the $\gamma^* p \rightarrow \gamma p$ forward scattering only the double-helicity-flip amplitudes can contribute to $d\sigma_L/dt$. Furthermore, we find that $d\sigma_T/dt$ is dominated by the b -type couplings and $d\sigma_L/dt$ is dominated by the a -type couplings.

In the middle panels of Fig. 3, we show the complete theoretical result and individual components contributing to the cross-section $d\sigma/dt$, see (15), for $W = 82$ GeV and $Q^2 = 8$ GeV² together with the H1 data [22]. The contributions of soft \mathbb{P} (the blue short-dashed lines), hard \mathbb{P} (the red long-dashed lines), the interference term (the green dotted lines), and their sum total (the thin full lines) for T and L components individually are also shown. The constructive interference of the soft and hard pomeron terms is a salient feature there.

In the bottom panels of Fig. 3 we show the ratios of the $\gamma^* p \rightarrow \gamma p$ cross-sections for longitudinally and transversely polarized virtual photons,

$$R(Q^2, W^2) = \frac{\sigma_L(Q^2, W^2)}{\sigma_T(Q^2, W^2)}, \quad \tilde{R}(Q^2, W^2, t) = \frac{\frac{d\sigma_L}{dt}(Q^2, W^2, t)}{\frac{d\sigma_T}{dt}(Q^2, W^2, t)}, \quad (16)$$

as functions of Q^2 and $|t|$, respectively. The cross-section σ_L vanishes proportionally to Q^2 for $Q^2 \rightarrow 0$. The ratio $\tilde{R}(Q^2, W^2, t)$ strongly grows with $|t|$. We must emphasize that this behaviour of $\tilde{R}(Q^2, W^2, t)$ depends crucially on our (reasonable) assumption that a and b couplings in the $\mathbb{P}_j \gamma^* \gamma^*$ vertex functions have the same t dependence for a given j .

In [25, 26] also the Regge theory was applied to DVCS. These authors consider only leading helicity amplitudes (only transversely polarized initial γ^* 's). In contrast, in our tensor-pomeron approach we present a complete model (all helicity amplitudes). Therefore, we could make, e.g., predictions for σ_L/σ_T which can and should be checked by experiments. The contribution of the interference term found in [26] is considerable for intermediate values of Q^2 , but smaller than our findings.

4. Conclusions

The two-tensor-pomeron model proposed previously to describe low x DIS data [2] was applied to deeply virtual Compton scattering (DVCS) for high c.m. energies W and small Bjorken x , say $x \lesssim 0.02$ [1].

In particular, the transition from the small- Q^2 regime, including the photoproduction ($Q^2 = 0$) limit, to the large- Q^2 regime, the DIS limit is well described. We compared predictions of the two-tensor-pomeron model to the DVCS data measured at HERA. We considered FIT 1 in which a 'minimal' modification of the Q^2 dependence of only one $\gamma^*(Q^2)\gamma\mathbb{P}$ coupling function was made. We considered also FIT 2 in which the size of the hard-pomeron component was increased, especially for larger Q^2 , and the soft-pomeron component was reduced relative to FIT 1. We kept here, on purpose, the same parameters of the form factors (14) as in FIT 1. The FIT 2 better describes the data at larger $|t|$ for $Q^2 \gtrsim 8 \text{ GeV}^2$ (see Fig. 3).

The model describes the W , Q^2 and t dependences of $d\sigma(\gamma^*p \rightarrow \gamma p)/dt$ measured at HERA and of the elastic photon-proton cross-section measured at FNAL. A good description of the DVCS data is achieved due to a sizeable interference of soft and hard pomeron contributions. The soft component and also the interference of soft and hard terms are very important up to at least $Q^2 \simeq 20 \text{ GeV}^2$.

Our calculation include the contributions of both the transverse and longitudinal virtual photons. The longitudinal cross-section $d\sigma_L/dt$ is predicted to be very small for $|t| \rightarrow 0$ but to be sizeable for $0.5 \text{ GeV}^2 \lesssim |t| \lesssim 1.0 \text{ GeV}^2$. We give also predictions for σ_L/σ_T which can and should be checked by experiments. The corresponding ratio of L/T grows strongly with $|t|$. We showed the Q^2 dependence of this ratio for different c.m. energies of the γ^*p system.

We presented predictions for low- x DVCS of the two-tensor-pomeron model which previously was successfully applied to low x DIS in [2]. The model provides amplitudes for all helicity configurations and, thus, can be checked by experimentalists in many ways. We are looking forward to further tests of the non-perturbative QCD dynamics embodied in our tensor-pomeron exchanges in future electron-hadron collisions in the low- x regime at the EIC [4] and LHeC [5] colliders.

Acknowledgments

P.L. thanks the organizers of XXIX Cracow Epiphany Conference for a well-organized conference with many stimulating discussions. This work was partially supported by the Polish National Science Centre Grant No. 2018/31/B/ST2/03537.

REFERENCES

- [1] P. Lebedowicz, O. Nachtmann, A. Szczurek, *Phys. Lett. B* **835**, 137497 (2022).
- [2] D. Britzger, C. Ewerz, S. Glazov, O. Nachtmann, and S. Schmitt, *Phys. Rev. D* **100** 114007 (2019).
- [3] M. Diehl, *Phys. Rept.* **388**, 41 (2003).
- [4] R. Abdul Khalek *et al.*, *Nucl. Phys. A* **1026**, 122447 (2022).
- [5] P. Agostini *et al.*, (LHeC, FCC-he Study Group), *J. Phys. G* **48**, 110501 (2021).
- [6] C. Ewerz, M. Maniatis, and O. Nachtmann, *Annals Phys.* **342**, 31 (2014).
- [7] C. Ewerz, P. Lebedowicz, O. Nachtmann, and A. Szczurek, *Phys. Lett. B* **763**, 382 (2016).
- [8] A. Donnachie and P. V. Landshoff, *Phys. Lett. B* **437**, 408 (1998).
- [9] P. Lebedowicz, O. Nachtmann, A. Szczurek, *Annals Phys.* **344**, 301 (2014).
- [10] P. Lebedowicz, O. Nachtmann, A. Szczurek, *Phys. Rev. D* **91**, 074023 (2015).
- [11] P. Lebedowicz, O. Nachtmann, A. Szczurek, *Phys. Rev. D* **93**, 054015 (2016).
- [12] P. Lebedowicz, O. Nachtmann, A. Szczurek, *Phys. Rev. D* **97**, 094027 (2018).
- [13] P. Lebedowicz, O. Nachtmann, A. Szczurek, *Phys. Rev. D* **99**, 094034 (2019).
- [14] P. Lebedowicz, O. Nachtmann, A. Szczurek, *Phys. Rev. D* **101**, 094012 (2020).
- [15] P. Lebedowicz, O. Nachtmann, A. Szczurek, *Phys. Rev. D* **102**, 114003 (2020).
- [16] P. Lebedowicz, O. Nachtmann, A. Szczurek, *Phys. Rev. D* **105**, 014022 (2022).
- [17] P. Lebedowicz, O. Nachtmann, A. Szczurek, *Phys. Rev. D* **106**, 034023 (2022).
- [18] P. Lebedowicz, O. Nachtmann, A. Szczurek, arXiv: 2302.07192 [hep-ph].
- [19] T. Arens, O. Nachtmann, M. Diehl, and P. V. Landshoff, *Z. Phys. C* **74**, 651 (1997).
- [20] A. M. Breakstone *et al.*, *Phys. Rev. Lett.* **47**, 1778 (1981).
- [21] A. Aktas *et al.*, (H1 Collaboration), *Eur. Phys. J. C* **44**, 1 (2005).
- [22] F. D. Aaron *et al.*, (H1 Collaboration), *Phys. Lett. B* **681**, 391 (2009).
- [23] S. Chekanov *et al.*, (ZEUS Collaboration), *Phys. Lett. B* **573**, 46 (2003).
- [24] S. Chekanov *et al.*, (ZEUS Collaboration), *JHEP* **05**, 108 (2009).
- [25] M. Capua, S. Fazio, R. Fiore, L. L. Jenkovszky, and F. Paccanoni, *Phys. Lett. B* **645**, 161 (2007).
- [26] S. Fazio, R. Fiore, L. Jenkovszky, and A. Sali, *Phys. Rev. D* **90**, 016007 (2014).

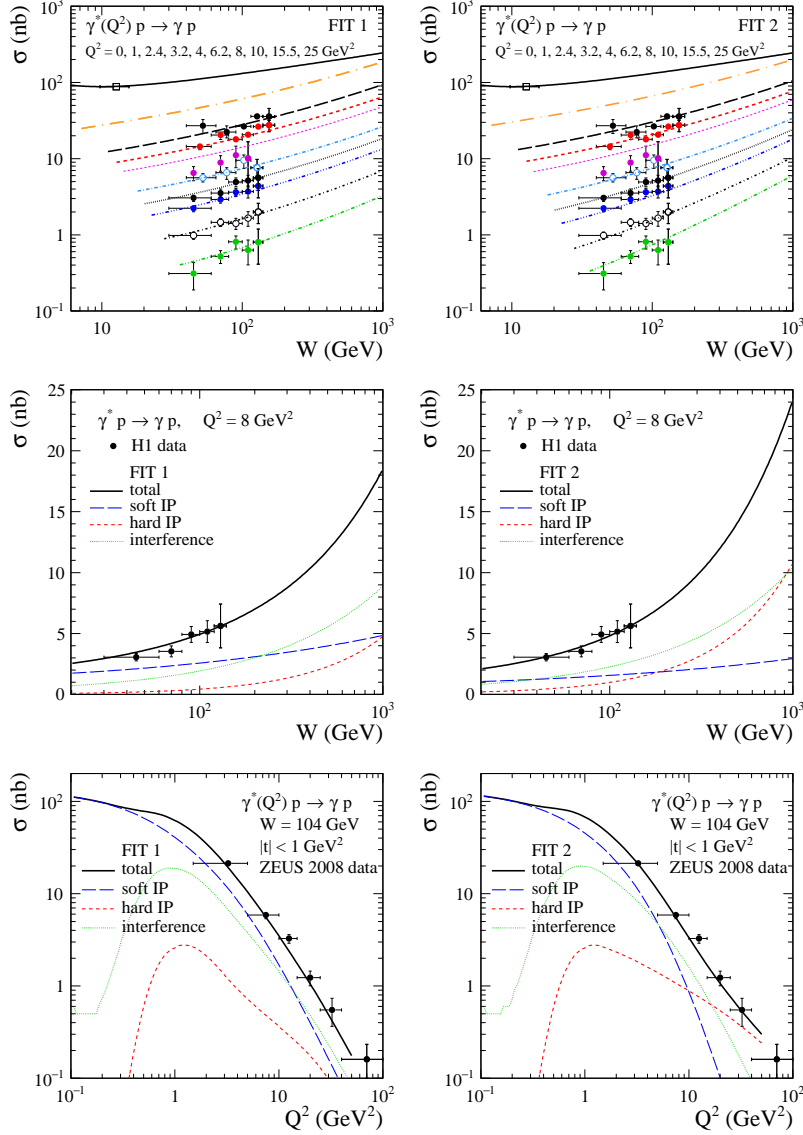


Fig. 2. **Top panels:** Total cross-sections as a function of the c.m. energy W for FIT 1 (left) and FIT 2 (right). Comparison of theoretical results to the FNAL data from [20] for real Compton scattering ($Q^2 = 0$) and to the DVCS HERA data is shown. The upper black solid line is for $Q^2 = 0$, the orange long-dashed-dotted line is for $Q^2 = 1 \text{ GeV}^2$. The remaining lines correspond to the values $Q^2 = 2.4, 3.2, 4, 6.2, 8, 10, 15.5, 25 \text{ GeV}^2$ (from top to bottom) and should be compared with the HERA data from [21–24]. **Middle panels:** Fit results for $Q^2 = 8 \text{ GeV}^2$ together with the H1 data [22]. The interference term of soft and hard pomeron is shown by the green dotted line. **Bottom panels:** Comparison of cross-sections as a function of Q^2 to the ZEUS data from [24].

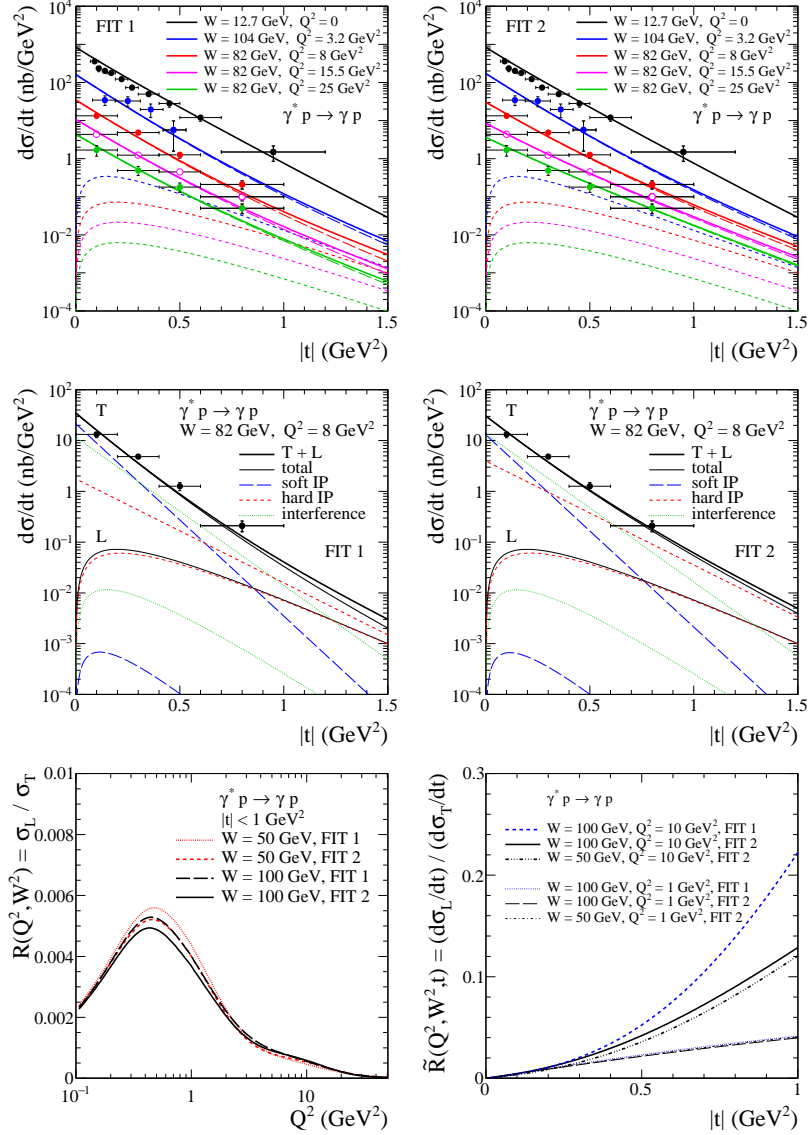


Fig. 3. **Top panels:** The differential cross-sections $d\sigma/dt$ for FIT 1 (left) and FIT 2 (right) compared to experimental data for different W and Q^2 . The upper line corresponds to $W = 12.7$ GeV and $Q^2 = 0$ and averaged FNAL data [20]. The bottom lines correspond to theoretical results for $\gamma^* p \rightarrow \gamma p$ at higher Q^2 for transverse (long-dashed lines) and longitudinal (short-dashed lines) polarization of the γ^* and their sum (solid lines). Data for $\langle W \rangle = 104$ GeV are from [24] and for $\langle W \rangle = 82$ GeV from [22]. **Middle panels:** Comparison of the results for $\gamma^* p \rightarrow \gamma p$ for transverse (T) and longitudinal (L) polarization of the γ^* individually and their sum T + L (see the upper solid lines) to DVCS H1 data [22] for $W = 82$ GeV and $Q^2 = 8$ GeV². **Bottom panels:** The ratios (16) for the $\gamma^* p \rightarrow \gamma p$ reaction. Note that the meaning of the lines on these two panels is different.